Estimating global ammonia (NH₃) emissions based on IASI observations from 2008 to 2018

Zhenqi Luo[1, 2], Yuzhong Zhang[1, 2, *], Wei Chen[1, 2], Martin van Damme[3, 4], Pierre-François Coheur[3], Lieven Clarisse[3]

[1]Key Laboratory of Coastal Environment and Resources of Zhejiang Province, School of Engineering, Westlake University, Hangzhou, Zhejiang Province, 310024, China
[2]Institute of Advanced Technology, Westlake Institute for Advanced Study, Hangzhou, Zhejiang Province, 310024, China
[3]Université libre de Bruxelles (ULB), Spectroscopy, Quantum Chemistry and Atmospheric Remote Sensing (SQUARES), Brussels, Belgium
[4]BIRA-IASB - Belgian Institute for Space Aeronomy, Brussels, Belgium

Correspondence to: Y. Zhang (zhangyuzhong@westlake.edu.cn), Z. Luo (zl725@cornell.edu)

Abstract. Emissions of ammonia (NH₃) to the atmosphere impact human health, climate, and ecosystems through their critical contributions to secondary aerosol formation. Estimation of NH₃ emissions is associated with large uncertainties because of inadequate knowledge about agricultural sources. Here, we use satellite observations from the Infrared Atmospheric Sounding Interferometer (IASI) and simulations from the GEOS-Chem model to constrain global NH₃ emissions over the period of 2008-2018. We update the prior NH₃ emission fluxes with the ratio between biases in simulated NH₃ concentrations and effective NH₃ lifetimes against the loss of the NH$_x$ family. In contrast to about a factor of two discrepancies between top-down and bottom-up emissions found in previous studies, our method results in a global land NH₃ emission of 78 (70-92) Tg a^{-1}, ~30 % higher than the bottom-up estimates. Regionally, we find that the bottom-up inventory underestimates NH₃ emissions over South America and tropical Africa by 60-70 %, indicating under-representation of agricultural sources in these regions. We find a good agreement within 10 % between bottom-up and top-down estimates over the U.S., Europe, and eastern China. Our results also show significant increases in NH₃ emissions over India (13 % decade^{-1}), tropical Africa (33 % decade^{-1}), and South America (18 % decade^{-1}) during our study period, consistent with the intensifying agricultural activities in these regions in the past decade. We find that inclusion of sulfur dioxide (SO₂) column observed by satellite is crucial for more accurate inference of NH₃ emission trends over important source regions such as India and China where SO₂ emissions have changed rapidly in recent years.

1 Introduction

Emissions of ammonia (NH₃) to the atmosphere have critical implications for human health, climate, and ecosystems. As the main alkaline gas, NH₃ reacts with acidic products from precursors such as nitrogen oxides (NO$_x$) and sulfur dioxide (SO₂) to form fine particulate matter, which is a well-documented risk factor for human health, causing great welfare loss globally

(Erisman 2021; Gu et al., 2021). Particulate matter also affects the Earth's radiative balance by directly scattering incoming radiation (Ma et al., 2012) and indirectly as cloud condensation nuclei (Höpfner et al., 2019). Additionally, both gas-phase ammonia (NH_3) and aerosol-phase ammonium (NH_4^+) can deposit onto the surface of land and water through dry and wet processes, and are associated with soil acidification (Zhao et al., 2009), ecosystem eutrophication (Dirnböck et al., 2013), biodiversity loss (Stevens et al., 2010), and cropland nitrogen uptake (Liu et al., 2013).

NH_3 is emitted from a variety of anthropogenic and natural sources, including agriculture, industry, fossil fuel combustion, biomass burning, natural soils, ocean, and wild animals (Behera et al., 2013). Among these, agricultural activities, mainly livestock manure management and mineral fertilizer application, are the most important NH_3 sources, which account for ~70% of the total NH_3 emissions globally (Bouwman et al., 1997; Sutton et al., 2013). NH_3 emissions can be estimated with a bottom-up approach based on information of emission activities and emission factors (Hoesly et al., 2018; Crippa et al., 2021). However, bottom-up estimates of NH_3 emissions are generally thought to be uncertain, relative to other pollutants that are mainly from fossil fuel combustion sources (e.g., NO_x, CO). One of the challenges is that the intensity of agricultural NH_3 emissions, emission factors, either from livestock or fertilizer, depends strongly on management and farming practices, but this information is usually not widely available (Zhang et al., 2017). Furthermore, microbial activities that are responsible for agricultural NH_3 emissions are highly variable and has a complex dependence on environmental conditions, which is often inadequately captured by bottom-up approaches (Behera et al., 2013; Vira et al., 2021). In many cases, emission factors used in bottom-up modelling are based on local studies that are not representative for the diversity of conditions and are not dependent on meteorological parameters.

Top-down analyses of atmospheric observations (e.g., NH_3 concentrations or NH_4^+ depositional fluxes) provide an alternative constraint on NH_3 emissions. For example, observations of NH_3 concentrations and NH_4^+ deposition fluxes from surface networks can be used to infer regional NH_3 emission fluxes (e.g., Paulot et al., 2014). However, surface sites are often sparse, especially in developing continents such as Africa and South America, limiting our capability to constrain NH_3 emissions globally. The advent of satellite observations makes it possible to investigate long-term spatially resolved NH_3 emissions from national, continental, to global scales. Van Damme et al. (2018) reported large NH_3 point sources across the globe that are detected by the Infrared Atmospheric Sounding Interferometer (IASI) instrument but missing in the bottom-up inventories. Studies have also applied satellite data (e.g., IASI and Cross-track Infrared Sounder (CrIS)) to study NH_3 emissions from important source regions, including the U.S. (Cao et al., 2020; Chen et al., 2021b), China (Zhang et al., 2018), and Europe (Marais et al., 2021; van der Graaf et al., 2021). These regional studies show 20 % to 50 % differences between top-down and bottom-up estimates of NH_3 emissions.

Compared to regional analyses, long-term global analyses of NH_3 emissions based on satellite observations are relatively scarce (e.g., Evangeliou et al., 2021). This is partly because of the computational challenges arising from a full-fledged inversion for a long period of time and over large spatial extents. In a recent study, Evangeliou et al. (2021) proposed a fast top-down method, in which NH_3 emissions are computed as the ratio between NH_3 column observations and NH_3 lifetime. This method relies on NH_3 lifetime diagnosed from a chemical transport model (CTM) and assumes a local mass balance.

67 Their analysis found a global NH_3 emission of around 180 Tg a^{-1}, which is roughly triple the widely used bottom-up
68 estimates (e.g., 62 Tg a^{-1} by the Community Emission Data System, CEDS). This large upward adjustment, if true, would
69 have huge implications for global reactive nitrogen cycles and indicate that our current understanding of global NH_3
70 emissions is seriously flawed.

71 In this paper, we examine if the large discrepancy between the bottom-up and top-down estimates is due to the methodology.
72 We refine the fast top-down approach by improving NH_3 lifetime diagnosis and partially accounting for the transport
73 contributions. We develop a series of data filtering procedures to exclude results that are not sufficiently constrained by
74 observations or affected by large deviations from the assumption of the fast top-down method. We apply the updated method
75 to IASI observations to derive the global distribution of NH_3 emissions fluxes from 2008 to 2018, and examine the impact of
76 the improved method on global NH_3 emission inferences.

2 Methods

2.1 IASI observations

79 We use 2008-2018 reanalyzed daily NH_3 total column retrievals (ANNI-NH_3-v3R) from the IASI on board Metop-A. The
80 IASI instrument measures the infrared radiation (645–2760 cm^{-1}) from Earth's surface and the atmosphere with a circular 12
81 km footprint at nadir (Clerbaux et al., 2009; Van Damme et al., 2017). The retrieval algorithm calculates the hyperspectral
82 range index from IASI spectra measurements (Van Damme et al. 2014) and converts it to the NH_3 total column density via
83 an artificial neural network (Whitburn et al., 2016; Franco et al., 2018). The retrieval uses consistent meteorological data
84 from the ERA5 reanalysis, so it is suitable for the analyses of inter-annual variability and long-term trends (Hersbach et al.,
85 2020). The ANNI-NH_3-v3R product, has been validated against in situ measurements and is shown to have a good regional
86 correlation (Guo et al., 2021; Van Damme et al., 2021). The dataset has been used in previous studies to estimate NH_3
87 emissions globally (e.g., Evangeliou et al., 2021) and regionally (e.g., Chen et al., 2021b; Marais et al., 2021).

88 Here we only use morning NH_3 data (around 9:30 local solar time) though IASI provides global coverage twice daily,
89 because of the better precision of morning observations resulting from favourable thermal contrast conditions (Clarisse et al.
90 2010). We filter out data with a cloud fraction greater than 10 % (Van Damme et al., 2018) and a skin temperature below
91 263 K (Van Damme et al., 2014). The skin temperature dataset is from ERA5 (Hersbach et al., 2020). To compare with
92 simulated NH_3 columns (see **Sect. 2.2**), we regrid and average monthly IASI NH_3 observations over land on the GEOS-
93 Chem 4° × 5° grid (**Fig. 1a**). To reduce uncertainty from sparse sampling, we further exclude grid cells with the number of
94 successful retrievals less than 800 in a month. We also test the choices of the threshold for 400 and 1200 per month in the
95 sensitivity calculations (**Table 1**, line 5-6). This criterion affects mainly high latitudes during wintertime, where snow
96 surfaces make it unfavourable for infrared measurements **(Fig. S1).**
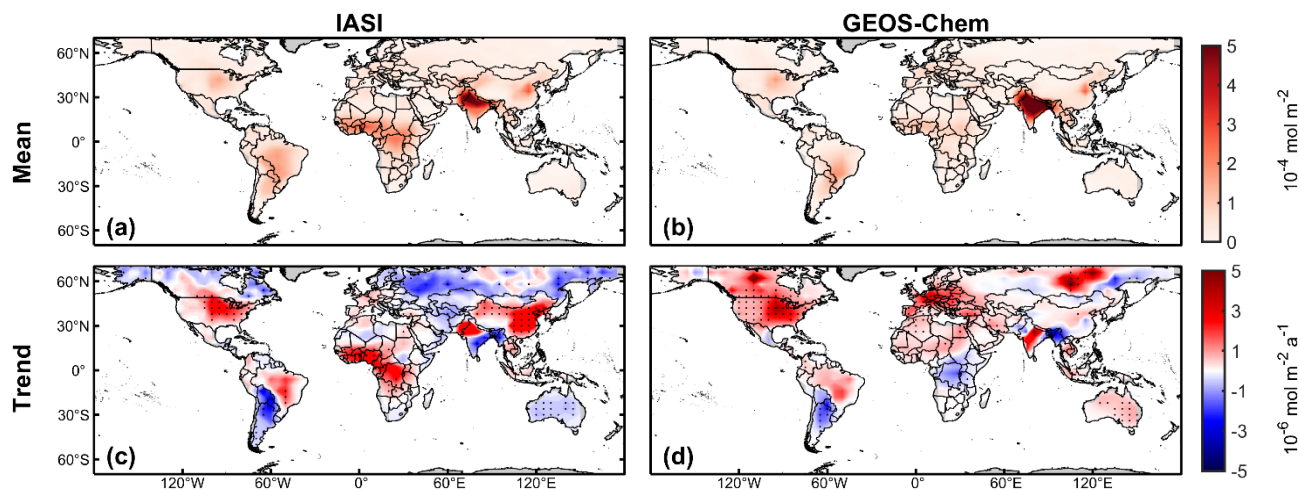
Figure 1. Spatial distribution of (a, c) IASI and (b, d) GEOS-Chem NH$_3$ column concentrations. (a, b) Mean and (c, d) linear trends within the **70**°N-**70**°S during 2008-2018. Dots in (c) and (d) indicate that linear trends are significant at the 95 % confidence levels. Linear trends are computed from the time series of annual averages.

2.2 GEOS-Chem simulations

We use the GEOS-Chem CTM v12.9.3 (10.5281/zenodo.3974569) to simulate global NH$_3$ concentrations. The GEOS-Chem model, driven by the MERRA-2 reanalyzed meteorology (Gelaro et al., 2017), simulates the tropospheric ozone–NOx–VOCs–aerosol chemistry at 4° × 5° resolution with 47 vertical layers (30 layers in the troposphere) (Bey et al., 2001; Park et al., 2004). The thermodynamic equilibrium between gas phase NH$_3$ and aerosol phase NH$_4^+$ is explicitly simulated by the ISORROPIA-II module in GEOS-Chem (Fountoukis & Nenes, 2007). The model also simulates the wet and dry deposition of NH$_3$ and NH$_4^+$, the terminal sinks of atmospheric NH$_x$ ($\equiv$ NH$_3$ + NH$_4^+$). Dry deposition is represented with a resistances-in-series scheme (Wesely, 2007) and wet deposition includes scavenging in convective updrafts and in- and below-cloud scavenging from large-scale precipitation (Wang et al., 2011; Amos et al., 2012). Anthropogenic emissions of simulated chemicals including those of NH$_3$ are taken from a global emission inventory CEDS (Hoesly et al., 2018), overridden by regional inventories in Canada (Air Pollutant Emission Inventory, APEI), the United States (2011 National Emissions Inventory, NEI-2011), Asia (MIX-Asia v1.1) (Li et al., 2017), and Africa (DICE-Africa) (Eloise Marais and Christine Wiedinmyer, 2016). Such compiled anthropogenic emissions only include incomplete information on inter-annual trends because inventories are not all available throughout the whole period. Anthropogenic emissions are essentially invariant after 2013 in our setup (**Fig. S2**). The general lack of trends in SO$_2$ emissions in the simulation, if not accounted for, may cause biases in inferred trends over regions such as India and China where SO$_2$ emissions have changed rapidly (Sun et al., 2018; Qu et al., 2019; Chen et al., 2021a). Fire emissions are from Global Fire Emissions Database (GFED4) (van der Werf et al., 2017), and biogenic VOC emissions are from the Model of Emissions of Gases and Aerosols from Nature (MEGAN) (Guenther et al., 2012). Temporal (seasonal and inter-annual) variations in fire and biogenic emissions are resolved by the inventories. Hereafter, we refer to NH$_3$ prior bottom-up emissions from this set of inventories as BUE1. For comparison, we

122 also use another set of bottom-up inventories which consist of EDGARv5.0 for anthropogenic emissions
123 (https://data.jrc.ec.europa.eu/collection/edgar, last access: 8 March 2022, Crippa et al., 2020), GFAS for fire emissions
124 (CAMS, https://apps.ecmwf.int/datasets/data/cams-gfas/, last access: 8 March 2022) (minor natural emissions are the same
125 as BUE1), which we denote as BUE2.

126 The GEOS-Chem simulation is conducted from 2008 to 2018 with an additional 1-month spin-up starting from December
127 2007. We sample the simulated NH_3 and NH_4^+ concentration fields between 9:00 to 10:00 local solar time, approximately the
128 IASI morning overpass time. To compare with the IASI NH_3 columns, we integrate the vertical profiles of simulated NH_3
129 concentrations by layer thickness. We note that the ANNI-NH_3-v3R algorithm does not involve averaging kernels (Whitburn
130 et al., 2016; Van Damme et al., 2021). Van Damme et al. (2018) reported the uncertainty in different vertical profiles of
131 individual NH_3 measurements to be 2 % $\pm$ 24 % (global average). We also archive simulated depositional and transport rates
132 for NH_3 and NH_4^+, which are used in emission fluxes estimation. In addition, we perform GEOS-Chem simulations in
133 selected years (2008, 2013, 2018) to examine the validation and consistency of our top-down NH_3 emission estimates with
134 the ground-based measurements and IASI observations.

135 **2.3 NH_3 emission fluxes estimation**

136 We compute NH_3 fluxes ($\hat{E}_{NH_3}$, in molecules m^{-2} s^{-1}) in land grid cells for individual months from 2008 to 2018. We update
137 the prior model emission fluxes ($E_{NH_3,mod}$, in molecules m^{-2} s^{-1}) with a correction term positively proportional to the
138 difference of observed ($C_{NH_3,obs}$, in molecules m^{-2}) and simulated ($C_{NH_3,mod}$, in molecules m^{-2}) monthly averaged NH_3 total
139 column densities and inversely proportional to the lifetime of NH_3 ($\tau_{NH_3,mod}$, in s):

$$\hat{E}_{NH_3} = E_{NH_3,mod} + \frac{C_{NH_3,obs} - C_{NH_3,mod}}{\tau_{NH_3,mod}}, \qquad (1)$$

141 where $\tau_{NH_3,mod}$ is computed as the ratio of the simulated NH_3 column and the sum of simulated loss rate of the NH_x family
142 ($NH_x \equiv NH_3 + NH_4^+$) through the dry and wet depositions of NH_3 ($D_{NH_3,mod}$, in molecules m^{-2} s^{-1}) and NH_4^+ ($D_{NH_4^+,mod}$, in
143 molecules m^{-2} s^{-1}):

$$\tau_{NH_3,mod} = \frac{C_{NH_3,mod}}{D_{NH_3,mod} + D_{NH_4^+,mod}}. \qquad (2)$$

145 Here we calculate the lifetime of NH_3 with the loss of the NH_x family rather than that of NH_3, because of the fast
146 thermodynamic equilibrium between gas-phase NH_3 and aerosol/aqueous-phase NH_4^+, which implies that the conversion
147 from NH_3 to NH_4^+ is not a terminal loss for NH_3 from the atmosphere. The NH_3 lifetime may be underestimated over source
148 regions and overestimated over remote regions, if NH_3 to NH_4^+ conversions are treated as a terminal loss as in Evangeliou et
149 al. (2021) rather than a partition within a chemical family (NH_x) as in **Eq. (2)**.

150 In addition, our method linearizes the column-emission relationship at prior emissions as opposed to zero emissions in the
151 previous method (e.g., Evangeliou et al., 2021). Here, the baseline NH_3 column ($C_{NH_3,mod}$) simulated by the GEOS-Chem

152 model explicitly accounts for the non-local contribution of transport, while the correction to prior emissions is done only

153 locally, that is, the difference between $C_{\mathrm{NH_3,obs}}$ and $C_{\mathrm{NH_3,mod}}$ is attributed only to errors in local emissions without

154 accounting for the sensitivity to emissions from other grid cells. This hybrid approach can partially include the non-local

155 contribution from transport but still keeps the computation tractable for a long-term study such as this study, striking a trade-

156 off between the computational efficiency of a local mass balance method (e.g., Van Damme et al., 2018; Evangeliou et al.,

157 2021) and the accuracy of a full-fledged inversion, such as the 4D-Var method (e.g., Cao et al., 2020; Chen et al., 2021b).

158 The errors arising from local correction of NH_3 emissions are expected to be small in most cases, because the NH_3 lifetime is

159 short relative to a typical transport time across a $4° \times 5°$ grid cell on which emissions are estimated. To identify cases when

160 this error is not negligible, we apply a monthly NH_x budget analysis based on the GEOS-Chem simulation and exclude grid

161 cells from our analysis where transport dominates over local prior emissions or depositions in the monthly NH_x budget

162 (Transport/Emission>1 or Transport/Deposition>1) (**Fig. S3**).

163 Because rapid changes in SO_2 emissions in eastern China and India, particularly after 2012, are not captured by our prior

164 simulation (**Fig. S2**), the estimation of NH_3 emission trends using **Eq. (1)** may be biased over these regions. To address this

165 issue, we further modify **Eq. (1)** to include observed trends in SO_2 column concentrations:

$$166 \qquad \hat{E}_{\mathrm{NH_3,SO_2-correct}} = E_{\mathrm{NH_3,mod}} + \frac{C_{\mathrm{NH_3,obs}} - C_{\mathrm{NH_3,mod}} + 2\omega C_{SO_4^{2-},mod}}{\tau_{\mathrm{NH_3,mod}}}, \qquad (3)$$

167 where ω (%) is the fractional changes of average SO_2 columns relative to the baseline year (i.e., 2012) over China or India

168 and $C_{SO_4^{2-},mod}$ (molecules m^{-2} s^{-1}) is the simulated column densities of aerosol sulfate. Here, we specify a linear trend of -5 %

169 a^{-1} for eastern China and 5 % a^{-1} for India between 2012 and 2018, based on values derived from the ozone monitoring

170 instrument (OMI) and Ozone Mapping and Profiler Suite (OMPS) observations (Wang and Wang, 2020; Liu et al., 2018).

171 We also test the impact of the uncertainty in ω on trend inferences over China and India. The factor 2 accounts for the fact

172 that two molecules of NH_3 are required to neutralize one molecule of H_2SO_4. **Eq. (3)** only applies when NH_3 is in excess, a

173 condition usually met in eastern China and India but not necessarily elsewhere (Lachatre et al., 2019; Acharja et al., 2022).

174 Therefore, we only apply **Eq. (3)** to eastern China and India to understand the impact of changing SO_2 emissions on the

175 inference of NH_3 emission trends. To use SO_2 observations systematically in NH_3 emission estimations requires further

176 investigations.

177 **2.4 Uncertainty and sensitivity analysis**

178 We perform a series of perturbation and sensitivity experiments to assess the uncertainty of our estimates (**Table 1**. We

179 perturb $C_{\mathrm{NH_3,mod}}$ and $\tau_{\mathrm{NH_3,mod}}$ in **Eq. (1)**. The perturbations to $\tau_{\mathrm{NH_3,mod}}$ are set to be 50 % and 200 % (**Table 1**, Line 1-2).

180 The perturbation to $C_{\mathrm{NH_3,mod}}$ is set to be the standard deviation of monthly mean column concentrations ($\sigma_{\mathrm{C,obs}}$) (**Table 1**,

181 Line 3-4), which is given by:

182
$$\sigma_{C,obs} = \sqrt{\frac{\sum_{i=1}^{i=n}(\sigma_i \times \Omega_i)^2}{n-1}}, \qquad (4)$$

183 where Ω_i (in mol m^{-2}) is the ith NH$_3$ column measurement out of a total number of n observations in a grid cell during a

184 month and σ_i is the relative error. We then use $\Omega \pm \sigma_{C,obs}$ to evaluate the effect of measurement errors in emission estimates

185 (**Table 1**, Line 3-4). We compute results with alternative data filtering parameters (**Table 1**, Line 5-8), including the

186 thresholds to exclude grid cells when the number of observations is too small (**Table 1**, line 5-6) and the local mass balance

187 assumption is potentially invalid (**Table 1**, Line 7-8). We also test if our trend inferences over China and India using Eq. (3)

188 is sensitive to uncertainty in observed trends in SO$_2$ concentrations (ω).

189 **Table 1.** Uncertainty and sensitivity analyses of top-down NH$_3$ emissions. Annual averaged NH$_3$ emissions are summed over global land
190 areas for 2008–2018.

	Parameter perturbed	Average emission (Tg a^{-1})
0	None [a] (TDE)	78
1	Halved NH$_3$ lifetime[b]	92
2	Doubled NH$_3$ lifetime[c]	70
3	Upper IASI column error	83
4	Lower IASI column error	72
5	Number of retrievals > 400[d]	81
6	Number of retrievals > 1200[e]	74
7	Transport/Emission < 0.2[f]	72
8	Transport/Emission < 5[g]	84

191 [a]Excluding a grid cell if retrieval number is less than 800 during a month, or transport dominates over emissions or

192 depositions in the simulated monthly NH$_3$ budget.

193 [b-c]The lifetime is 50 % and 200 % of values from Eq. (1), respectively.

194 [d-e]Monthly retrieval number threshold for including a grid cell is set to be 400 and 1200, respectively.

195 [f-g]Local budget ratio the threshold for including a grid cell is set to be 0.2 and 5, respectively.

196 **3 Results and discussion**

197 **3.1 Observed and simulated NH$_3$ concentrations**

198 **Fig. 1a and 1b** plot observed and simulated NH$_3$ total column concentrations averaged over 2008-2018. The GEOS-Chem

199 simulation generally reproduces the global distribution of NH$_3$ concentrations observed by the IASI instrument. Good

200 agreements (i.e., difference < 10 %) are found in the U.S., Europe, and southern South America. Meanwhile, the GEOS-

Chem model underestimates NH_3 concentrations in eastern China, northern South America, and tropical Africa by 20-120 %, and overestimates in southern India by around 50 %, indicating biases in NH_3 emissions over these regions.

Fig. 1c and 1d show 2008-2018 linear trends in NH_3 column concentrations derived from the IASI observations and the GEOS-Chem simulations. The linear trends are computed based on the time series of annual averages. The IASI trends shown in Fig. 1c are in general consistent with a recent analysis by Van Damme et al. (2021). IASI observes a positive NH_3 concentration trend of 2.9 % a^{-1} over the U.S., and this trend is well captured by GEOS-Chem. Similarly, the observation and the simulation agree on a dipole pattern in South America (i.e., positive trend in Brazil and negative trend in Argentina). Because anthropogenic emissions over this region are set to be invariant in our simulation (**Fig. S2**), this agreement suggests that these trends are due to meteorological conditions and/or fire emissions, rather than changes in anthropogenic emissions. The satellite also observes significant positive trends in NH_3 concentrations over China (5.2 % a^{-1}) and tropical Africa (2.0 % a^{-1}), but these trends are not reproduced in the simulation (0.3 % a^{-1} for China and 0.2 % a^{-1} for tropical Africa). These simulation-observation differences can not only reflect discrepancies in the trends of anthropogenic NH_3 emissions, but also be attributed to uncaptured changes in SO_2 and/or NO_x emissions in these regions. We also find that a positive NH_3 concentration trend over Europe appears in the simulation (3.0 % a^{-1}) but is much weaker (1.0 % a^{-1}) in the observation, suggesting decreasing emissions after 2013. Satellite data shows positive NH_3 concentration trends in north-western India but negative trends in in south-eastern India which are not reproduced by the simulation, though these trends over India are mostly insignificant (at the 95 % confidence level) except for a few grid cells in the Southeast. Strong GEOS-Chem trends in eastern Canada and Siberia result from large wildfires that occurred in the latter part of the study period. IASI trends in northern boreal regions are less robust because of noisy and sparse measurements over high latitudes (**Fig. S1** and **Fig. S3**)

3.2 NH_3 emissions inferred from IASI observations

Fig. 2 shows the spatial distributions of NH_3 emission fluxes and their 2008–2018 linear trends inferred from IASI observations using the method described in **Sect. 2.3**. **Fig. 3** plots annual time series aggregated for seven selected regions. The top-down emission (TDE) estimates suggest upward adjustments in NH_3 emissions over South America (SA) by 62 %, tropical Africa (TA) by 69 %, and Central Asia (CA) by 327 %, relative to the prior inventory (BUE1), but downward adjustments in NH_3 emissions by 14 % in India Peninsula (IP) and by 33 % in Canada. After accounting for the contributions from natural emissions including fires, we find that most of these biases in NH_3 emissions can be attributed to anthropogenic sources, except for Canada where the underestimation appears to relate to fire emissions. This result reflects a general inadequate representation of agricultural and industrial emissions from developing continents in current global emission inventories. The TDE finds good agreements with the BUE1 (difference within 10 %) over the U.S., Europe (EU), eastern China (EC) and Australia.
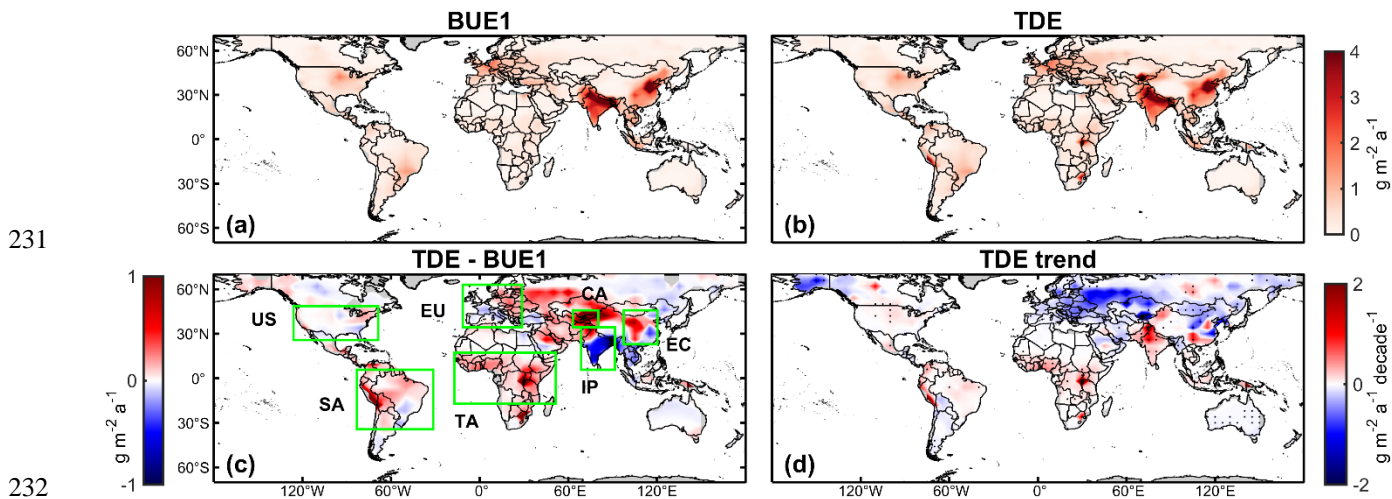
Figure 2. Spatial distribution of NH₃ emission fluxes during 2008-2018. (a) Bottom-up emissions (BUE1), (b) top-down emissions (TDE) inferred from IASI observations, (c) difference between TDE and BUE1 estimates and (d) emission trends derived from TDE estimates. Green boxes denote seven regions analyzed in Sect. 3.2. Top-down emission fluxes are computed with Eq. (1) except for IP and EC where Eq. (3) is applied. Linear trends are computed from the time series of annual averages. Dots in (d) represent significant linear trends at the 95 % confidence level.

In addition to the adjustments in average emissions, the TDE also detects changes in NH₃ emissions during the period of 2008-2018, as expressed in linear trends computed from annual time series. We find significant positive emission trends in SA (1.7 Tg a⁻¹ decade⁻¹ or 18 % decade⁻¹) and TA (2.8 Tg a⁻¹ decade⁻¹ or 33 % decade⁻¹) (**Fig. 3**). The large positive trends in TA are found around Lake Natron, consistent with Clarisse et al. (2019) (Fig. 2d). These increases in NH₃ emissions are concurrent with intensifying agricultural activities in these regions (Warner et al., 2017; E. Hickman et al., 2020), except for a 2010 peak over SA, which coincides with fires in savanna and evergreen forests there (Chen et al., 2013). Comparison with data from the Food and Agriculture Organization of the United Nations (FAO) (http://www.fao.org/faostat, last access: 7 May 2022) suggests that the increase in SA is driven primarily by growing application of synthetic fertilizer (55 % decade⁻¹), whereas the increase in TA is consistent with increasing manure amount (28 % decade⁻¹) from a growing livestock population (E. Hickman et al., 2021) (**Fig. 4**).

Our results infer large but variable trends over northern high latitudes (e.g., negative trends in Alaska, central Russia, and eastern Europe, but positive trends in Canada) (**Fig. 2d**). Because of large uncertainties associated with high-latitude observations and emission optimization, these trends are less robust but can be partly attributed to variations in fire activities. Decreases in Russia and eastern Europe are related to wildfire of boreal forests in early part of the study period (2008-2011) (Keywood et al., 2012; Warner et al., 2017), while emission increases in Canada is due to wildfire in the late part of the period (2013-2016 and 2017) (Pavlovic et al., 2016), as also shown in the prior fire inventory (GFED4) (**Fig. S4**). We also infer negative trends (-43 % decade⁻¹) in Australia, which are statistically significant, but the absolute magnitude of these trends is small (-0.03 g m⁻² a⁻¹ decade⁻¹ in **Fig. 2d**). The TDE estimation does not find significant trends in NH₃ total emissions over the US and Central Asia.

257
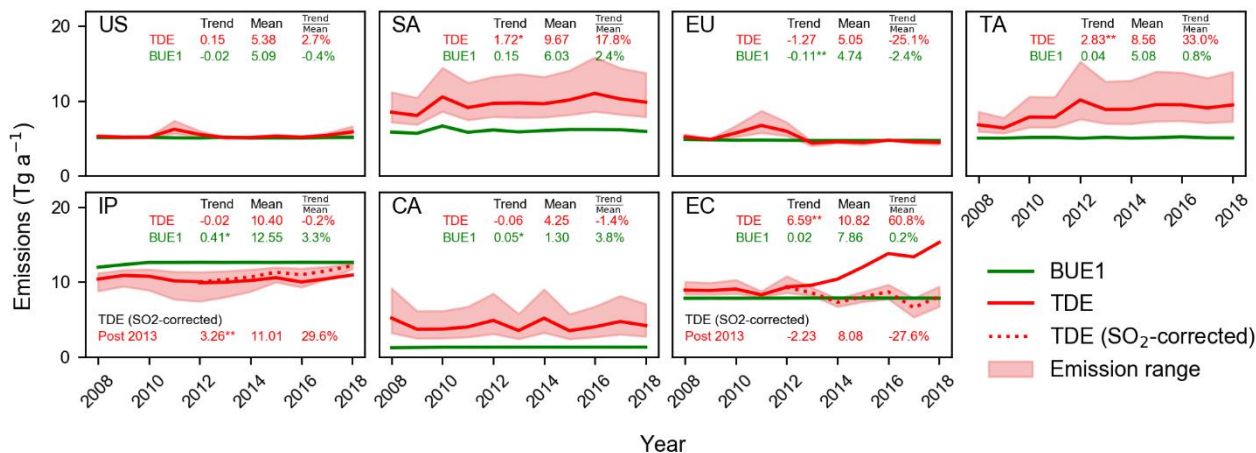
Figure 3. Annual NH$_3$ emissions for seven selected regions during 2008-2018. Shadings represent the upper and lower bounds derived from uncertainty analyses (see Sect. 2.4). Average annual emissions (Tg a^{-1}), absolute linear trends (Tg a^{-1} decade^{-1}) and relative trends (% decade^{-1}) for 2008-2018 are inset. The asterisk symbols '*' and '**' represent that linear trends are significant at the 95 % and 99 % confidence level, respectively. Red dashed lines represent top-down NH$_3$ emission estimates over IP and EC during 2013-2018, based on Eq. (3) that accounts for observed trends of SO$_2$ (denoted as "SO$_2$-corrected"). Statistics for this estimate are also inset. The prior inventory (BUE1) implemented in our simulation only partially account for inter-annual changes from bottom-up information (i.e., **Fig. 4**).

264
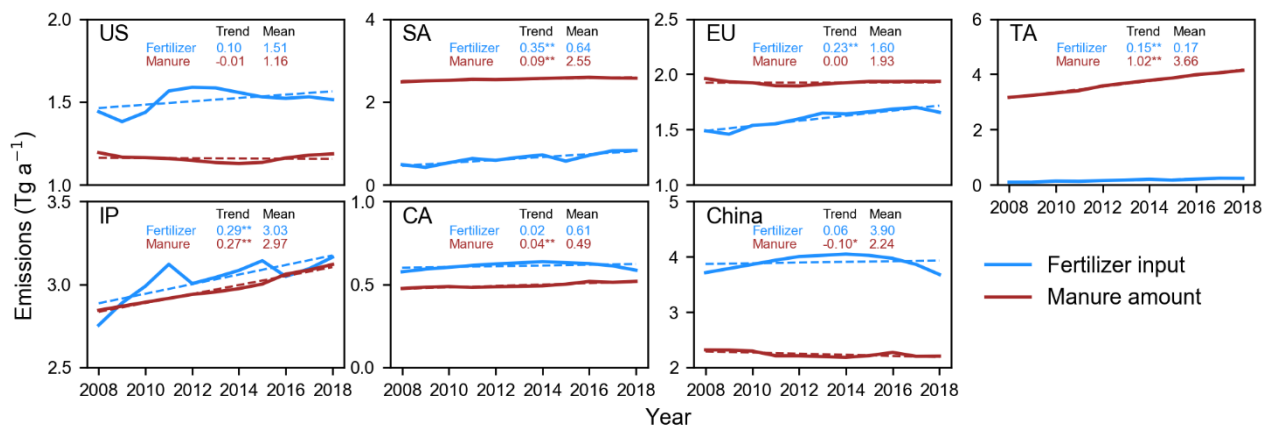
Figure 4. Synthetic fertilizer and livestock manure amount based on FAO reports (http://www.fao.org/faostat) during 2008-2018. To roughly compare the contribution from the two sectors, we convert FAO reported statistics to NH$_3$ emissions (Tg a^{-1}) by applying fixed emission factors of 13 % for manure N contents (Ma et al., 2020) and 17 % for synthetic fertilizer N contents (Riddick et al., 2016). Values of means (Tg a^{-1}) and linear trends (Tg a^{-1} decade^{-1}) are inset. Scales differ between panels.

3.3 Impact of changing SO$_2$ emissions on NH$_3$ emission trends over eastern China and India

Based on NH$_3$ column measurements (**Eq. (1)**), we also find a decadal increase of 61 % decade^{-1} (6.6 Tg a^{-1} decade^{-1}) in NH$_3$ emissions over eastern China (**Fig. 3**). This increase is especially large after 2013 and is driven mainly by increases of IASI NH$_3$ column concentration in eastern China (**Fig. 1c**). This large post-2013 increase is inconsistent with flat or even declining fertilizer input and manure amount (**Fig. 4**). On the other hand, we find no appreciable emission trend in IP (**Fig.**

274   **3**), which appears to agree with relatively stable IASI NH$_3$ concentrations over the period (**Fig. 1c**) but is not supported by

275   increases in fertilizer applications and manure amount shown in the FAO report (**Fig. 4**).

276   An assumption underlying **Eq. (1)** is that the model simulation captures the partition between gas-phase NH$_3$ and aerosol-

277   phase NH$_4^+$. In addition to alkaline NH$_3$, the partition is also determined by the abundance of acids (e.g., H$_2$SO$_4$ and HNO$_3$).

278   Inaccurate emissions of their precursors (e.g., SO$_2$ and NO$_2$) in the model simulation, in particular over regions with

279   excessive NH$_3$, can lead to biases in simulating the NH$_3$-NH$_4^+$ partition. It is well known that SO$_2$ emissions in China have

280   decreased rapidly after 2013 because of stringent air pollution control measures (Sun et al., 2018; Zhai et al., 2021), while

281   SO$_2$ emissions from India have been increasing (Qu et al., 2019). But these regional trends are not captured in our prior

282   simulation because our simulation does not have annual-varying emission inventories for these regions (**Fig. S2**).

283   We find that the discrepancies between top-down (**Eq. 1**) and bottom-up estimates of emission trends over EC and IP can be

284   largely reconciled by including observed SO$_2$ column concentrations in the top-down calculation (**Eq. (3)**). By accounting

285   for OMI and OMPS observed SO$_2$ trends (Wang and Wang, 2020), we derive an overall decreasing trend in NH$_3$ emissions

286   in EC between 2013 and 2018 (-2.2 $\pm$ 2.3 Tg a^{-1} decade^{-1}, -28 $\pm$ 32 % decade^{-1}) (uncertainty derived by perturbing ω by 1%

287   a^{-1}, same for the India results below). This result suggests that observed increases in NH$_3$ columns over China are largely

288   explained by decreases in SO$_2$ emissions (**Fig. 1** and **Fig. 3**), consistent with previous studies (Fu et al., 2017; Liu et al.,

289   2018; Lachatre et al., 2019; Chen et al., 2021a). Bottom-up inventories (e.g., MEIC v1.3, EDGAR v5.0) also report stable or

290   declining NH$_3$ emissions from China during the period (Li et al., 2017; Crippa et al., 2020). Meanwhile, the revised method

291   (**Eq. (3)**) finds a positive post-2013 trend (3.3 $\pm$ 0.3 Tg a^{-1} decade^{-1}, 30 $\pm$ 3 % yr^{-1}) in NH$_3$ emissions over India. Compared

292   with our original estimate using **Eq. (1)**, NH$_3$ emission trends derived with **Eq. (3)** (i.e., decrease in China and increase in

293   India after 2013) is more consistent with the bottom-up information of fertilizer input and manure management (**Fig. 4**). This

294   result demonstrates the potential of assimilating both NH$_3$ and SO$_2$ satellite observations in constraining NH$_3$ emissions,

295   which should be further explored in the future.

296   **3.4 Global total NH$_3$ emissions**

297   Integrating over land areas globally, our IASI-based TDE estimates of NH$_3$ is 78 (70-92) Tg a^{-1} (range of estimates from

298   uncertainty analysis, see **Table 1**) (**Fig. 5**). This result is about 20-40 % higher than bottom-up inventories (BUE1, 62 Tg a^{-1}

299   and BUE2, 56 Tg a^{-1}). In contrast, a previous study by Evangeliou et al. (2021) also based on the IASI data estimated a much

300   higher global NH$_3$ emission of 180 Tg a^{-1} (**Fig. 5**). One cause of the difference between the two IASI-based estimates is in

301   diagnosis of NH$_3$ lifetime from CTM. Evangeliou et al. (2021) treats conversion from NH$_3$ to NH$_4^+$ as a terminal loss and

302   diagnoses NH$_3$ lifetime averaged 11.6 $\pm$ 0.6 h globally from a CTM, which is close to a constant NH$_3$ lifetime (12 h)

303   assumed in Van Damme et al. (2018). In this study, we account for the fact that fast thermodynamic equilibrium can

304   establish between NH$_3$ and NH$_4^+$ so that NH$_3$ can only be terminally lost through the deposition of the NH$_x$ family (**Eq. (2)**),

305   which yields a global averaged NH$_3$ lifetime of 21.2 $\pm$ 3.8 h (**Fig. 6**). This longer NH$_3$ lifetime implies a higher sensitivity of

306   NH$_3$ column density to NH$_3$ emissions, leading to a lower estimate for global NH$_3$ emissions. In addition, instead of locally

307 scaling observed NH₃ column by lifetime (Van Damme et al., 2018; Evangeliou et al, 2021; Marais et al., 2021), our method
308 (**Eq. (1)**) partially accounts for the non-local contribution from transport by including prior NH₃ columns from a full 3-D
309 simulation and using their difference from observed NH₃ columns to correct prior emissions, which prevents derivation of
310 large NH₃ emissions in remote regions where observed NH₃ concentrations are driven mainly by transport. Our data filtering
311 strategy (**Sect 2.1 and 2.2**) is also crucial to avoid spurious top-down results when satellite coverage is poor and the local
312 mass balance assumption does not hold.
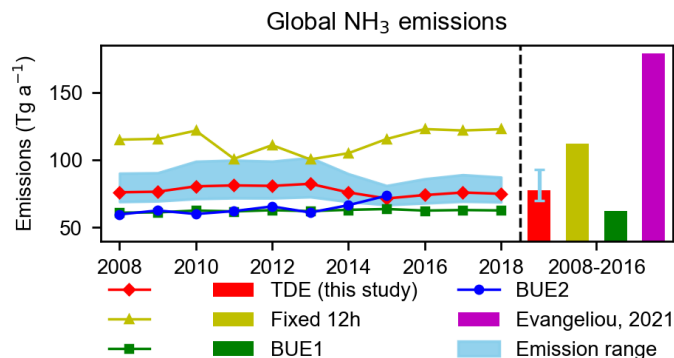
313

314 **Figure 5.** Comparison of our top-down NH₃ emission estimates (TDE) with other top-down (Fixed 12h and Evangeliou et al. (2021)) and
315 bottom-up (BUE1 and BUE2) results during 2008-2018. The red line and red bar represent central estimates of the TDE, and the blue
316 shaded area and the blue error bar indicate the uncertainty evaluated by our study (**Sect. 2.4**).
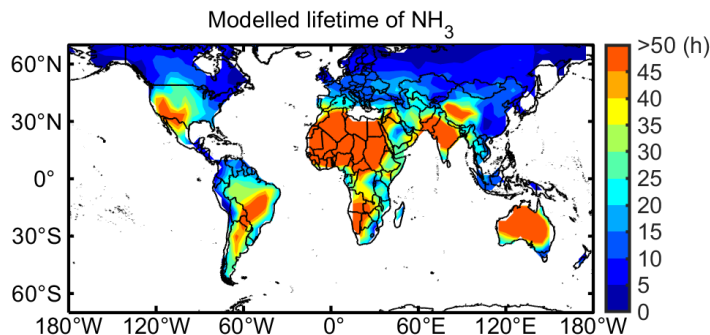
317

318 **Figure 6.** Spatial distribution of NH₃ lifetime (h) diagnosed from GEOS-Chem (Eq. (2)) within the **70°N-70°S** during 2008-2018.

319 **Fig. 6** shows the spatial variation in NH₃ lifetime diagnosed from the GEOS-Chem simulation. Short NH₃ lifetimes (< 10 h)
320 are found mainly in northern high latitudes. Short lifetime in eastern China is due to high wet NH_4^+ deposition velocity,
321 although some regional studies suggested an overestimation of deposition fluxes by the model especially in forest areas (e.g.,
322 Yangtze River basin) (Zhao et al., 2017; Xu et al., 2018). Very long NH₃ lifetime (> 100 h) occurs over Sahara and
323 Australia, where dry conditions result in slow wet deposition.

3.5 Uncertainty evaluation

We derive the uncertainty of top-down estimates from the perturbation tests in **Table 1**. **Fig. 7** shows the global spatial distribution of annual average uncertainties of NH_3 emissions derived from the ensemble of these perturbation tests. Absolute uncertainties are expressed as half of the ensemble ranges, and relative uncertainties are computed by normalizing absolute uncertainties by ensemble averages. We find that both absolute and relative uncertainties are large in Central Asia and Tropical Africa, indicating that these source regions are not well constrained by observations. In comparison, observations have some constraints over important source regions of eastern China and northern India, which have small relative uncertainties (< 20 %) but still appreciable absolute uncertainties (> 0.4 g a^{-1} m^{-2}). Uncertainties are small (< 20 % and/or < 0.2 g a^{-1} m^{-2}) in Europe and the U.S.
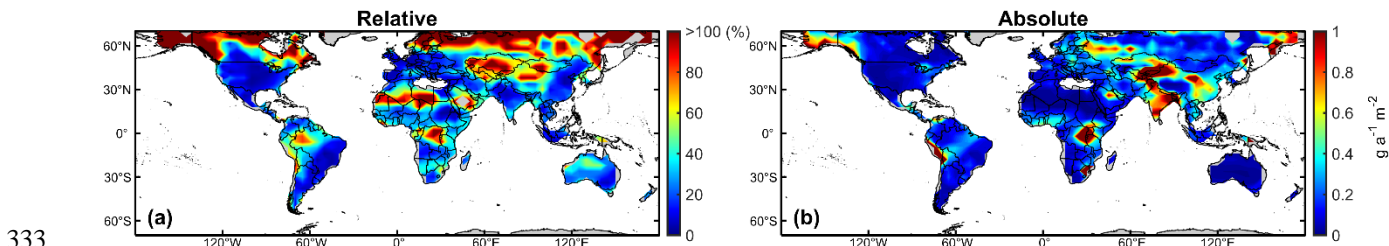
Figure 7. Spatial distribution of TDE (a) relative and (b) absolute uncertainty during 2008-2018. Absolute uncertainties are derived as half of the perturbation ensemble range (**Table 1**) and relative uncertainties are computed by normalizing absolute uncertainties with ensemble averages.

Our fast top-down method (Eq. (1) and Eq. (3)) relies on simplification of NH_3 chemical and physical processes. Therefore, it is not guaranteed that a simulation driven by TDE will generate results in improved agreement with IASI observations. We evaluate the consistency of our results using full GEOS-Chem simulations in the selected years of 2008, 2013, and 2018. Results are shown in **Fig. S5** (fractional bias, FB) and **Table S1** (number of valid grid cells, R^2, and root mean square error). The GEOS-Chem simulations driven by the prior emissions (BUE1) tends to underestimate NH_3 column density (mean FB ~-30%), while that driven by our TDE estimates achieves lower biases (mean FB ~10%), demonstrating the consistency of our TDE results with IASI observations.

3.6 Comparison to independent surface networks

We also compare simulated surface NH_3 concentrations with independent ground-based measurements, including (1) biweekly averaged NH_3 concentrations in North America (AMoN, https://nadp.slh.wisc.edu/networks/ammonia-monitoring-network/, last access: 3 June 2022), (2) half-hourly/daily/weekly averaged NH_3 concentrations in (EMEP, http://ebas-data.nilu.no/, last access: 3 June 2022), and (3) monthly averaged NH_3 concentrations in south-eastern Asia (EANET, https://www.eanet.asia/, last access: 3 June 2022). AMoN measures NH_3 concentrations by passive devices (simple diffusion-type simpler), while EMEP and EANET use both active and passive sampler systems among different sites (multi-type samplers). For comparison, we convert the observed NH_3 concentrations in μg m^{-3} to ppbv using a factor of 1.44

352   (assume 25 °C temperature and 1 atmosphere pressure) and average observations monthly over the GEOS-Chem 4° × 5°
353   grid. **Fig. 8** shows the comparison by season. Only small adjustments are inferred by our satellite-based estimations in these
354   regions (i.e., North America, Europe, and South-eastern Asia). Thus, TDE and BUE1 show similar performance against
355   these ground measurements. Although the simulation can capture the site-to-site variations reasonably well, simulated
356   surface values are in general biased low compared to observations. This low bias is also reported in the evaluation of
357   previous IASI-based estimates (e.g., Evangeliou et al, 2021; Chen et al., 2021b). Further investigations are needed to
358   understand the reasons for this bias.
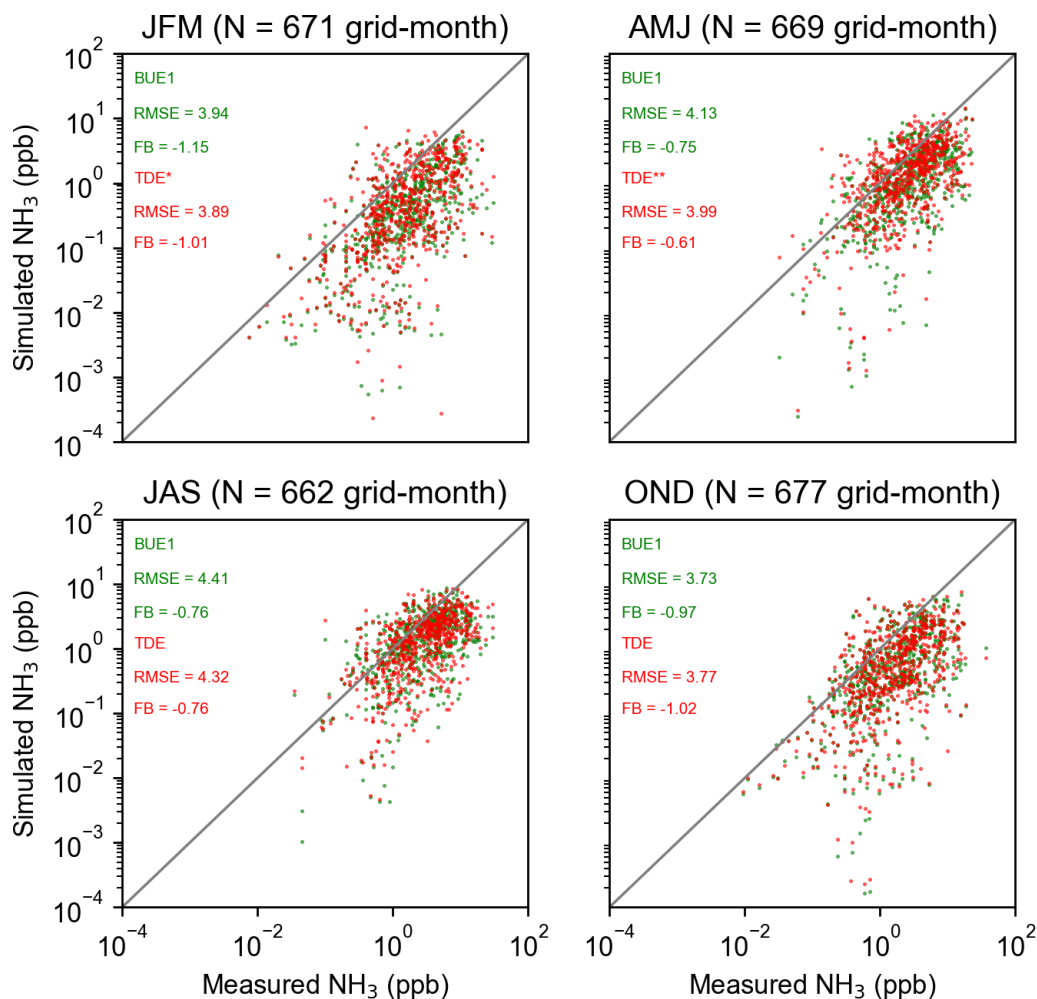
359

360   **Figure 8.** Validation of simulated NH_3 concentrations driven by BUE1 and TDE against ground-based measurements from AMoN,
361   EMEP, EANET for selected years (2008, 2013 and 2018) in four seasons (January-March, JFM; April-June, AMJ; July-September, JAS;
362   October-December, OND). Scatterplots are plotted in log scale and average RMSE (ppb) and FB (%) for each season are inset. The
363   asterisk symbols '*' and '**' represent that differences between BUE1 and TDE are significant at the 95 % and 99 % confidence level.

4 Conclusions

This study quantifies global ammonia (NH_3) fluxes monthly from 2008 to 2018 at $4° \times 5°$ resolution, through a fast top-down method that incorporates IASI satellite observations and GEOS-Chem model simulations. The top-down method updates the prior NH_3 emissions with a correction term positively proportional to the difference of the observed and simulated NH_3 concentrations, and inversely proportional to the lifetime diagnosed from a CTM. This method revises previously proposed fast top-down methods in two aspects. First, we account for thermodynamic equilibrium within the NH_x family in diagnosing NH_3 lifetime, while previous studies either assume a globally constant lifetime or treat conversion from NH_3 to NH_4^+ as a terminal sink. Second, our formulation linearizes the column-emission relationship at prior emissions as opposed to zero emissions in the previous method, which in general reduces errors from the local mass balance approximation. Another improvement is that we apply several data filtering procedures to exclude unreliable top-down results that are not sufficiently constrained by observations or affected by large deviations from the local mass balance assumption. The top-down method developed in this study is particularly useful for long-term global analysis of emission trends, because it largely accounts for the impact of meteorology through the CTM simulation and requires only small amount of computation relative to a full-fledged inversion.

We apply this improved fast top-down method to IASI NH_3 column observations from 2008 to 2018. We find that the BUE1 underestimates NH_3 emission over South America (62 %) and tropical Africa (69 %), but overestimates over India (14 %) and Canada (33 %). The bottom-up inventory agrees with the top-down estimate over the U.S., Europe, and eastern China (i.e., within 10 %). Our analysis also shows significant increases in India (13 % decade^{-1}), tropical Africa (33 % decade^{-1}), and South America (18 % decade^{-1}) during the study period, consistent with intensifying agricultural activities over these regions. An analysis of agricultural statistics suggests that the increase in tropical Africa is likely driven by growing livestock population and that in South America by increasing fertilizer usage.

We show that large increases in NH_3 concentrations in eastern China is mainly driven by rapid decreases in SO_2 emissions in recent years. By accounting for observed SO_2 columns, we find that NH_3 emissions from eastern China are significantly decreasing during 2008-2018 (-19 % decade^{-1}), with a larger negative trend after 2013 (-28 % decade^{-1}), as compared to a significant positive trend (61 % decade^{-1}) derived from assimilating only NH_3 data. Similarly, a lack of trend in observed NH_3 concentrations over India is due to concurrent increases in SO_2 and NH_3 emissions. After including observed SO_2 columns in the calculation, we estimate a 13 % increase in NH_3 emissions over India, with a significant post-2013 positive trend (30 % decade^{-1}). These results from assimilating both NH_3 and SO_2 data is more consistent with the agricultural statistics in China and India. The multi-satellite (SO_2 and NH_3) method is only applied in India and China in this study. To extend this idea globally requires development of formulations for varied sulfate-nitrate-ammonium aerosol regimes and needs to be addressed in a future study.

Our estimate for global total NH_3 emission is 78 (70-92) Tg a^{-1}, about 30 % higher than the BUE1 estimate. This contrasts with a much higher estimate (180 Tg a^{-1}) derived from Evangeliou et al. (2021) also using IASI data. The discrepancy can be

397 primarily attributed to a longer NH$_3$ lifetime (i.e., global average 21 h) diagnosed in our method, which represents a greater
398 sensitivity of NH$_3$ column to emissions, and a more conservative data filtering strategy, which removes potentially unreliable
399 top-down results. Our diagnosis of NH$_3$ lifetime is an improvement over Evangeliou et al. (2021), by accounting for the
400 thermodynamic equilibrium between gas phase NH$_3$ and aerosol phase NH$_4^+$ in our formula. We show with model
401 simulations, our top-down estimate achieves better consistency with IASI observations, compared to the bottom-up emission
402 inventory.

403

404 *Data availability.*

405 The IASI L2 ammonia satellite observations are available at the AERIS data infrastructure (https://iasi.aeris-data.fr/). The
406 ERA5 skin temperature and GFAS fire emission can be request through Copernicus Climate Data Store
407 (https://cds.climate.copernicus.eu/cdsapp#!/home). Agricultural data are available through Food and Agriculture
408 Organization of the United Nations (FAO) (http://www.fao.org/faostat). The GEOS-Chem model can be retrieved from
409 10.5281/zenodo.3974569. All the other data and scripts used for the present publication are available under MIT license on
410 GitHub: https://github.com/bnulzq/NH3-emission.git.

411 *Author contributions.*

412 ZL and YZ designed the study. ZL performed the simulations and analyses and wrote and coordinated the paper. WC
413 contributed to the model simulations for consistency evaluation. LC, MVD, and PFC developed the IASI-NH3 satellite
414 product. ZL and YZ wrote the paper with inputs from all authors.

415 *Competing interests*

416 The contact author has declared that neither they nor their co-authors have any competing interests.

417 *Acknowledgements.*

418 This study is supported by Westlake University. We thank the High-Performance Computing Center of Westlake University
419 for the facility support and technical assistance. We acknowledge the AERIS data infrastructure https://www.aeris-data.fr for
420 providing access to the IASI data. The IASI L1c data are received through the EUMETCast near real-time data distribution
421 service. Research at ULB was supported by the Belgian State Federal Office for Scientific, Technical and Cultural Affairs
422 (Prodex HIRS) and the Air Liquide Foundation (TAPIR project). LC is Research Associate supported by the Belgian F.R.S.-
423 FNRS. Hersbach et al., (2020) was downloaded from the Copernicus Climate Change Service (C3S) Climate Data Store. The
424 results contain modified Copernicus Climate Change Service information 2020. Neither the European Commission nor
425 ECMWF is responsible for any use that may be made of the Copernicus information or data it contains. IASI is a join
426 mission of Eumetsat and the "Centre National d'Études Spatiales" (CNES, France). We acknowledge the constructive

427 comments and suggestions from Prof. Peter Hess from the Cornell University, Dr. Yi Wang from the University of Iowa, and

428 Dr. Shixian Zhai from Harvard University. We also acknowledge Dr. Nikolaos Evangeliou from Norwegian Institute for Air

429 Research for providing his NH$_3$ emission flux data and for discussions with ZL.

References

431 Acharja, P., Ali, K., Ghude, S. D., Sinha, V., Sinha, B., Kulkarni, R., Gultepe, I., and Rajeevan, M. N.:
432 Enhanced secondary aerosol formation driven by excess ammonia during fog episodes in Delhi, India,
433 Chemosphere, 289, 133155, 10.1016/j.chemosphere.2021.133155, 2022.

434 Amos, H. M., Jacob, D. J., Holmes, C. D., Fisher, J. A., Wang, Q., Yantosca, R. M., Corbitt, E. S.,
435 Galarneau, E., Rutter, A. P., Gustin, M. S., Steffen, A., Schauer, J. J., Graydon, J. A., Louis, V. L. S.,
436 Talbot, R. W., Edgerton, E. S., Zhang, Y., and Sunderland, E. M.: Gas-particle partitioning of
437 atmospheric Hg(II) and its effect on global mercury deposition, Atmospheric Chemistry and Physics,
438 12, 591-603, 10.5194/acp-12-591-2012, 2012.

439 Behera, S. N., Sharma, M., Aneja, V. P., and Balasubramanian, R.: Ammonia in the atmosphere: a
440 review on emission sources, atmospheric chemistry and deposition on terrestrial bodies, Environ Sci
441 Pollut Res Int, 20, 8092-8131, 10.1007/s11356-013-2051-9, 2013.

442 Bey, I., Jacob, D. J., Yantosca, R. M., Logan, J. A., Field, B. D., Fiore, A. M., Li, Q., Liu, H. Y.,
443 Mickley, L. J., and Schultz, M. G.: Global modeling of tropospheric chemistry with assimilated
444 meteorology: Model description and evaluation, Journal of Geophysical Research: Atmospheres, 106,
445 23073-23095, 10.1029/2001jd000807, 2001.

446 Bouwman, A. F., Lee, D. S., Asman, W. A. H., Dentener, F. J., Van Der Hoek, K. W., and Olivier, J. G.
447 J.: A global high-resolution emission inventory for ammonia, Global Biogeochemical Cycles, 11, 561-
448 587, 10.1029/97gb02266, 1997.

449 Cao, H., Henze, D. K., Shephard, M. W., Dammers, E., Cady-Pereira, K., Alvarado, M., Lonsdale, C.,
450 Luo, G., Yu, F., Zhu, L., Danielson, C. G., and Edgerton, E. S.: Inverse modeling of NH3 sources using
451 CrIS remote sensing measurements, Environmental Research Letters, 15, 10.1088/1748-9326/abb5cc,
452 2020.

453 Chen, Y., Morton, D. C., Jin, Y., Collatz, G. J., Kasibhatla, P. S., van der Werf, G. R., DeFries, R. S.,
454 and Randerson, J. T.: Long-term trends and interannual variability of forest, savanna and agricultural
455 fires in South America, Carbon Management, 4, 617-638, 10.4155/cmt.13.61, 2014.

456 Chen, Y., Zhang, L., Henze, D. K., Zhao, Y., Lu, X., Winiwarter, W., Guo, Y., Liu, X., Wen, Z., Pan,
457 Y., and Song, Y.: Interannual variation of reactive nitrogen emissions and their impacts on PM2.5 air
458 pollution in China during 2005–2015, Environmental Research Letters, 16, 10.1088/1748-9326/ac3695,
459 2021a.

Chen, Y., Shen, H., Kaiser, J., Hu, Y., Capps, S. L., Zhao, S., Hakami, A., Shih, J.-S., Pavur, G. K., Turner, M. D., Henze, D. K., Resler, J., Nenes, A., Napelenok, S. L., Bash, J. O., Fahey, K. M., Carmichael, G. R., Chai, T., Clarisse, L., Coheur, P.-F., Van Damme, M., and Russell, A. G.: High-resolution hybrid inversion of IASI ammonia columns to constrain US ammonia emissions using the CMAQ adjoint model, Atmospheric Chemistry and Physics, 21, 2067-2082, 10.5194/acp-21-2067-2021, 2021b.

Clarisse, L., Van Damme, M., Gardner, W., Coheur, P. F., Clerbaux, C., Whitburn, S., ... & Hurtmans, D. (2019). Atmospheric ammonia (NH_3) emanations from Lake Natron's saline mudflats. Scientific reports, 9(1), 1-12.

Clerbaux, C., Boynard, A., Clarisse, L., George, M., Hadji-Lazaro, J., Herbin, H., Hurtmans, D., Pommier, M., Razavi, A., Turquety, S. J. A. C., and Physics: Monitoring of atmospheric composition using the thermal infrared IASI/MetOp sounder, Atmospheric Chemistry and Physics, 9, 6041-6054, 2009.

Crippa, M., Solazzo, E., Huang, G., Guizzardi, D., Koffi, E., Muntean, M., Schieberle, C., Friedrich, R., and Janssens-Maenhout, G.: High resolution temporal profiles in the Emissions Database for Global Atmospheric Research, Sci Data, 7, 121, 10.1038/s41597-020-0462-2, 2020.

Dirnbock, T., Grandin, U., Bernhardt-Romermann, M., Beudert, B., Canullo, R., Forsius, M., Grabner, M. T., Holmberg, M., Kleemola, S., Lundin, L., Mirtl, M., Neumann, M., Pompei, E., Salemaa, M., Starlinger, F., Staszewski, T., and Uzieblo, A. K.: Forest floor vegetation response to nitrogen deposition in Europe, Glob Chang Biol, 20, 429-440, 10.1111/gcb.12440, 2014.

Erisman, J. W. J. S.: How ammonia feeds and pollutes the world, Science, 374, 685-686, 2021.

Evangeliou, N., Balkanski, Y., Eckhardt, S., Cozic, A., Van Damme, M., Coheur, P.-F., Clarisse, L., Shephard, M. W., Cady-Pereira, K. E., and Hauglustaine, D.: 10-year satellite-constrained fluxes of ammonia improve performance of chemistry transport models, Atmospheric Chemistry and Physics, 21, 4431-4451, 10.5194/acp-21-4431-2021, 2021.

Fountoukis, C., Nenes, A. J. A. C., and Physics: ISORROPIA II: a computationally efficient thermodynamic equilibrium model for K^+–Ca^{2+}–Mg^{2+}–NH_4^+–Na^+–SO_4^{2-}–NO_3^-–Cl^-–H_2O aerosols, Atmospheric Chemistry and Physics, 7, 4639-4659, 2007.

Franco, B., Clarisse, L., Stavrakou, T., Müller, J. F., Van Damme, M., Whitburn, S., Hadji-Lazaro, J., Hurtmans, D., Taraborrelli, D., Clerbaux, C., and Coheur, P. F.: A General Framework for Global Retrievals of Trace Gases From IASI: Application to Methanol, Formic Acid, and PAN, Journal of Geophysical Research: Atmospheres, 123, 10.1029/2018jd029633, 2018.

Fu, X., Wang, S., Xing, J., Zhang, X., Wang, T., and Hao, J.: Increasing Ammonia Concentrations Reduce the Effectiveness of Particle Pollution Control Achieved via SO2 and NOX Emissions Reduction in East China, Environmental Science & Technology Letters, 4, 221-227, 10.1021/acs.estlett.7b00143, 2017.

Gelaro, R., McCarty, W., Suarez, M. J., Todling, R., Molod, A., Takacs, L., Randles, C., Darmenov, A., Bosilovich, M. G., Reichle, R., Wargan, K., Coy, L., Cullather, R., Draper, C., Akella, S., Buchard, V., Conaty, A., da Silva, A., Gu, W., Kim, G. K., Koster, R., Lucchesi, R., Merkova, D., Nielsen, J. E., Partyka, G., Pawson, S., Putman, W., Rienecker, M., Schubert, S. D., Sienkiewicz, M., and Zhao, B.: The Modern-Era Retrospective Analysis for Research and Applications, Version 2 (MERRA-2), J Clim, Volume 30, 5419-5454, 10.1175/JCLI-D-16-0758.1, 2017.

Gu, B., Zhang, L., Van Dingenen, R., Vieno, M., Van Grinsven, H. J., Zhang, X., Zhang, S., Chen, Y., Wang, S., and Ren, C. J. S.: Abating ammonia is more cost-effective than nitrogen oxides for mitigating PM2. 5 air pollution, Science, 374, 758-762, 2021.

Guenther, A. B., Jiang, X., Heald, C. L., Sakulyanontvittaya, T., Duhl, T., Emmons, L. K., and Wang, X.: The Model of Emissions of Gases and Aerosols from Nature version 2.1 (MEGAN2.1): an extended and updated framework for modeling biogenic emissions, Geoscientific Model Development, 5, 1471-1492, 10.5194/gmd-5-1471-2012, 2012.

Guo, X., Wang, R., Pan, D., Zondlo, M. A., Clarisse, L., Van Damme, M., Whitburn, S., Coheur, P. F., Clerbaux, C., Franco, B., Golston, L. M., Wendt, L., Sun, K., Tao, L., Miller, D., Mikoviny, T., Müller, M., Wisthaler, A., Tevlin, A. G., Murphy, J. G., Nowak, J. B., Roscioli, J. R., Volkamer, R., Kille, N., Neuman, J. A., Eilerman, S. J., Crawford, J. H., Yacovitch, T. I., Barrick, J. D., and Scarino, A. J.: Validation of IASI Satellite Ammonia Observations at the Pixel Scale Using In Situ Vertical Profiles, Journal of Geophysical Research: Atmospheres, 126, 10.1029/2020jd033475, 2021.

Hersbach, H., Bell, B., Berrisford, P., Hirahara, S., Horányi, A., Muñoz-Sabater, J., Nicolas, J., Peubey, C., Radu, R., Schepers, D., Simmons, A., Soci, C., Abdalla, S., Abellan, X., Balsamo, G., Bechtold, P., Biavati, G., Bidlot, J., Bonavita, M., Chiara, G., Dahlgren, P., Dee, D., Diamantakis, M., Dragani, R., Flemming, J., Forbes, R., Fuentes, M., Geer, A., Haimberger, L., Healy, S., Hogan, R. J., Hólm, E., Janisková, M., Keeley, S., Laloyaux, P., Lopez, P., Lupu, C., Radnoti, G., Rosnay, P., Rozum, I., Vamborg, F., Villaume, S., and Thépaut, J. N.: The ERA5 global reanalysis, Quarterly Journal of the Royal Meteorological Society, 146, 1999-2049, 10.1002/qj.3803, 2020.

Hickman, J. E., Andela, N., Tsigaridis, K., Galy-Lacaux, C., Ossohou, M., and Bauer, S. E.: Reductions in NO2 burden over north equatorial Africa from decline in biomass burning in spite of growing fossil fuel use, 2005 to 2017, Proc Natl Acad Sci U S A, 118, 10.1073/pnas.2002579118, 2021a.

Hickman, J. E., Andela, N., Dammers, E., Clarisse, L., Coheur, P.-F., Van Damme, M., Di Vittorio, C. A., Ossohou, M., Galy-Lacaux, C., Tsigaridis, K., and Bauer, S. E.: Changes in biomass burning, wetland extent, or agriculture drive atmospheric NH$_3$; trends in select African regions, Atmospheric Chemistry and Physics, 21, 16277-16291, 10.5194/acp-21-16277-2021, 2021b.

Hoesly, R. M., Smith, S. J., Feng, L., Klimont, Z., Janssens-Maenhout, G., Pitkanen, T., Seibert, J. J., Vu, L., Andres, R. J., Bolt, R. M., Bond, T. C., Dawidowski, L., Kholod, N., Kurokawa, J.-i., Li, M., Liu, L., Lu, Z., Moura, M. C. P., O'Rourke, P. R., and Zhang, Q.: Historical (1750–2014) anthropogenic

532 emissions of reactive gases and aerosols from the Community Emissions Data System (CEDS),
533 Geoscientific Model Development, 11, 369-408, 10.5194/gmd-11-369-2018, 2018.

534 Höpfner, M., Ungermann, J., Borrmann, S., Wagner, R., Spang, R., Riese, M., Stiller, G., Appel, O.,
535 Batenburg, A. M., Bucci, S., Cairo, F., Dragoneas, A., Friedl-Vallon, F., Hünig, A., Johansson, S.,
536 Krasauskas, L., Legras, B., Leisner, T., Mahnke, C., Möhler, O., Molleker, S., Müller, R., Neubert, T.,
537 Orphal, J., Preusse, P., Rex, M., Saathoff, H., Stroh, F., Weigel, R., and Wohltmann, I.: Ammonium
538 nitrate particles formed in upper troposphere from ground ammonia sources during Asian monsoons,
539 Nature Geoscience, 12, 608-612, 10.1038/s41561-019-0385-8, 2019.

540 Keywood, M., Kanakidou, M., Stohl, A., Dentener, F., Grassi, G., Meyer, C. P., Torseth, K., Edwards,
541 D., Thompson, A. M., Lohmann, U., and Burrows, J.: Fire in the Air: Biomass Burning Impacts in a
542 Changing Climate, Critical Reviews in Environmental Science and Technology, 43, 40-83,
543 10.1080/10643389.2011.604248, 2011.

544 Lachatre, M., Fortems-Cheiney, A., Foret, G., Siour, G., Dufour, G., Clarisse, L., Clerbaux, C., Coheur,
545 P.-F., Van Damme, M., and Beekmann, M.: The unintended consequence of SO_2 and NO_2; regulations
546 over China: increase of ammonia levels and impact on $PM_{2.5}$; concentrations, Atmospheric Chemistry
547 and Physics, 19, 6701-6716, 10.5194/acp-19-6701-2019, 2019.

548 Li, M., Zhang, Q., Kurokawa, J.-i., Woo, J.-H., He, K., Lu, Z., Ohara, T., Song, Y., Streets, D. G.,
549 Carmichael, G. R., Cheng, Y., Hong, C., Huo, H., Jiang, X., Kang, S., Liu, F., Su, H., and Zheng, B.:
550 MIX: a mosaic Asian anthropogenic emission inventory under the international collaboration
551 framework of the MICS-Asia and HTAP, Atmospheric Chemistry and Physics, 17, 935-963,
552 10.5194/acp-17-935-2017, 2017.

553 Liu, M., Huang, X., Song, Y., Xu, T., Wang, S., Wu, Z., Hu, M., Zhang, L., Zhang, Q., Pan, Y., Liu, X.,
554 and Zhu, T.: Rapid SO_2; emission reductions significantly increase tropospheric ammonia
555 concentrations over the North China Plain, Atmospheric Chemistry and Physics, 18, 17933-17943,
556 10.5194/acp-18-17933-2018, 2018.

557 Liu, X., Zhang, Y., Han, W., Tang, A., Shen, J., Cui, Z., Vitousek, P., Erisman, J. W., Goulding, K.,
558 Christie, P., Fangmeier, A., and Zhang, F.: Enhanced nitrogen deposition over China, Nature, 494, 459-
559 462, 10.1038/nature11917, 2013.

560 Ma, R., Zou, J., Han, Z., Yu, K., Wu, S., Li, Z., Liu, S., Niu, S., Horwath, W. R., and Zhu-Barker, X.:
561 Global soil-derived ammonia emissions from agricultural nitrogen fertilizer application: A refinement
562 based on regional and crop-specific emission factors, Glob Chang Biol, 27, 855-867,
563 10.1111/gcb.15437, 2021.

564 Ma, X., Yu, F., and Luo, G.: Aerosol direct radiative forcing based on GEOS-Chem-APM and
565 uncertainties, Atmospheric Chemistry and Physics, 12, 5563-5581, 10.5194/acp-12-5563-2012, 2012.

566 Marais, E. A. and Wiedinmyer, C.: Air Quality Impact of Diffuse and Inefficient Combustion Emissions
567 in Africa (DICE-Africa), Environ Sci Technol, 50, 10739-10745, 10.1021/acs.est.6b02602, 2016.

Marais, E. A., Pandey, A. K., Van Damme, M., Clarisse, L., Coheur, P. F., Shephard, M. W., Cady-Pereira, K. E., Misselbrook, T., Zhu, L., Luo, G., and Yu, F.: UK Ammonia Emissions Estimated With Satellite Observations and GEOS-Chem, Journal of Geophysical Research: Atmospheres, 126, 10.1029/2021jd035237, 2021.

Park, R. J.: Natural and transboundary pollution influences on sulfate-nitrate-ammonium aerosols in the United States: Implications for policy, Journal of Geophysical Research, 109, 10.1029/2003jd004473, 2004.

Paulot, F., Jacob, D. J., Pinder, R. W., Bash, J. O., Travis, K., and Henze, D. K.: Ammonia emissions in the United States, European Union, and China derived by high-resolution inversion of ammonium wet deposition data: Interpretation with a new agricultural emissions inventory (MASAGE_NH3), Journal of Geophysical Research: Atmospheres, 119, 4343-4364, 10.1002/2013jd021130, 2014.

Pavlovic, R., Chen, J., Anderson, K., Moran, M. D., Beaulieu, P. A., Davignon, D., and Cousineau, S.: The FireWork air quality forecast system with near-real-time biomass burning emissions: Recent developments and evaluation of performance for the 2015 North American wildfire season, J Air Waste Manag Assoc, 66, 819-841, 10.1080/10962247.2016.1158214, 2016.

Qu, Z., Henze, D. K., Li, C., Theys, N., Wang, Y., Wang, J., Wang, W., Han, J., Shim, C., Dickerson, R. R., and Ren, X.: SO2 Emission Estimates Using OMI SO2 Retrievals for 2005-2017, J Geophys Res Atmos, 124, 8336-8359, 10.1029/2019JD030243, 2019.

Riddick, S., Ward, D., Hess, P., Mahowald, N., Massad, R., and Holland, E.: Estimate of changes in agricultural terrestrial nitrogen pathways and ammonia emissions from 1850 to present in the Community Earth System Model, Biogeosciences, 13, 3397-3426, 10.5194/bg-13-3397-2016, 2016.

Schiferl, L. D., Heald, C. L., Van Damme, M., Clarisse, L., Clerbaux, C., Coheur, P.-F., Nowak, J. B., Neuman, J. A., Herndon, S. C., Roscioli, J. R., and Eilerman, S. J.: Interannual variability of ammonia concentrations over the United States:

sources and implications, Atmospheric Chemistry and Physics, 16, 12305-12328, 10.5194/acp-16-12305-2016, 2016.

Stevens, C. J., Dupre, C., Dorland, E., Gaudnik, C., Gowing, D. J., Bleeker, A., Diekmann, M., Alard, D., Bobbink, R., Fowler, D., Corcket, E., Mountford, J. O., Vandvik, V., Aarrestad, P. A., Muller, S., and Dise, N. B.: Nitrogen deposition threatens species richness of grasslands across Europe, Environ Pollut, 158, 2940-2945, 10.1016/j.envpol.2010.06.006, 2010.

Sun, W., Shao, M., Granier, C., Liu, Y., Ye, C. S., and Zheng, J. Y.: Long-Term Trends of Anthropogenic SO2, NOx, CO, and NMVOCs Emissions in China, Earth's Future, 6, 1112-1133, 10.1029/2018ef000822, 2018.

Sutton, M. A., Reis, S., Riddick, S. N., Dragosits, U., Nemitz, E., Theobald, M. R., Tang, Y. S., Braban, C. F., Vieno, M., Dore, A. J., Mitchell, R. F., Wanless, S., Daunt, F., Fowler, D., Blackall, T. D.,

Milford, C., Flechard, C. R., Loubet, B., Massad, R., Cellier, P., Personne, E., Coheur, P. F., Clarisse, L., Van Damme, M., Ngadi, Y., Clerbaux, C., Skjoth, C. A., Geels, C., Hertel, O., Wichink Kruit, R. J., Pinder, R. W., Bash, J. O., Walker, J. T., Simpson, D., Horvath, L., Misselbrook, T. H., Bleeker, A., Dentener, F., and de Vries, W.: Towards a climate-dependent paradigm of ammonia emission and deposition, Philos Trans R Soc Lond B Biol Sci, 368, 20130166, 10.1098/rstb.2013.0166, 2013.

Van Damme, M., Whitburn, S., Clarisse, L., Clerbaux, C., Hurtmans, D., and Coheur, P.-F.: Version 2 of the IASI NH_3; neural network retrieval algorithm: near-real-time and reanalysed datasets, Atmospheric Measurement Techniques, 10, 4905-4914, 10.5194/amt-10-4905-2017, 2017.

Van Damme, M., Clarisse, L., Whitburn, S., Hadji-Lazaro, J., Hurtmans, D., Clerbaux, C., and Coheur, P. F.: Industrial and agricultural ammonia point sources exposed, Nature, 564, 99-103, 10.1038/s41586-018-0747-1, 2018.

Van Damme, M., Clarisse, L., Heald, C. L., Hurtmans, D., Ngadi, Y., Clerbaux, C., Dolman, A. J., Erisman, J. W., and Coheur, P. F.: Global distributions, time series and error characterization of atmospheric ammonia (NH_3) from IASI satellite observations, Atmospheric Chemistry and Physics, 14, 2905-2922, 10.5194/acp-14-2905-2014, 2014.

Van Damme, M., Clarisse, L., Franco, B., Sutton, M. A., Erisman, J. W., Wichink Kruit, R., van Zanten, M., Whitburn, S., Hadji-Lazaro, J., Hurtmans, D., Clerbaux, C., and Coheur, P.-F.: Global, regional and national trends of atmospheric ammonia derived from a decadal (2008–2018) satellite record, Environmental Research Letters, 16, 10.1088/1748-9326/abd5e0, 2021.

Van Damme, M., Clarisse, L., Dammers, E., Liu, X., Nowak, J. B., Clerbaux, C., Flechard, C. R., Galy-Lacaux, C., Xu, W., Neuman, J. A., Tang, Y. S., Sutton, M. A., Erisman, J. W., and Coheur, P. F.: Towards validation of ammonia (NH_3) measurements from the IASI satellite, Atmospheric Measurement Techniques, 8, 1575-1591, 10.5194/amt-8-1575-2015, 2015.

van der Graaf, S., Dammers, E., Segers, A., Kranenburg, R., Schaap, M., Shephard, M. W., and Erisman, J. W.: Data assimilation of CrIS NH_3; satellite observations for improving spatiotemporal NH_3; distributions in LOTOS-EUROS, Atmospheric Chemistry and Physics, 22, 951-972, 10.5194/acp-22-951-2022, 2022.

van der Werf, G. R., Randerson, J. T., Giglio, L., van Leeuwen, T. T., Chen, Y., Rogers, B. M., Mu, M., van Marle, M. J. E., Morton, D. C., Collatz, G. J., Yokelson, R. J., and Kasibhatla, P. S.: Global fire emissions estimates during 1997–2016, Earth System Science Data, 9, 697-720, 10.5194/essd-9-697-2017, 2017.

Vira, J., Hess, P., Ossohou, M., and Galy-Lacaux, C., 10.5194/acp-2021-538,

Wang, Q., Jacob, D. J., Fisher, J. A., Mao, J., Leibensperger, E. M., Carouge, C. C., Le Sager, P., Kondo, Y., Jimenez, J. L., Cubison, M. J., and Doherty, S. J.: Sources of carbonaceous aerosols and deposited black carbon in the Arctic in winter-spring: implications for radiative forcing, Atmospheric Chemistry and Physics, 11, 12453-12473, 10.5194/acp-11-12453-2011, 2011.

639 Wang, Y. and Wang, J.: Tropospheric SO2 and NO2 in 2012–2018: Contrasting views of two sensors
640 (OMI and OMPS) from space, Atmospheric Environment, 223, 10.1016/j.atmosenv.2019.117214, 2020.

641 Warner, J. X., Dickerson, R. R., Wei, Z., Strow, L. L., Wang, Y., and Liang, Q.: Increased atmospheric
642 ammonia over the world's major agricultural areas detected from space, Geophys Res Lett, 44, 2875-
643 2884, 10.1002/2016GL072305, 2017.

644 Wesely, M.: Parameterization of surface resistances to gaseous dry deposition in regional-scale
645 numerical models☆, Atmospheric Environment, 41, 52-63, 10.1016/j.atmosenv.2007.10.058, 2007.

646 Whitburn, S., Van Damme, M., Clarisse, L., Bauduin, S., Heald, C. L., Hadji-Lazaro, J., Hurtmans, D.,
647 Zondlo, M. A., Clerbaux, C., and Coheur, P. F.: A flexible and robust neural network IASI-
648 NH3retrieval algorithm, Journal of Geophysical Research: Atmospheres, 121, 6581-6599,
649 10.1002/2016jd024828, 2016.

650 Xu, W., Zhao, Y., Liu, X., Dore, A. J., Zhang, L., Liu, L., and Cheng, M.: Atmospheric nitrogen
651 deposition in the Yangtze River basin: Spatial pattern and source attribution, Environ Pollut, 232, 546-
652 555, 10.1016/j.envpol.2017.09.086, 2018.

653 Zhai, S., Jacob, D. J., Wang, X., Liu, Z., Wen, T., Shah, V., Li, K., Moch, J. M., Bates, K. H., Song, S.,
654 Shen, L., Zhang, Y., Luo, G., Yu, F., Sun, Y., Wang, L., Qi, M., Tao, J., Gui, K., Xu, H., Zhang, Q.,
655 Zhao, T., Wang, Y., Lee, H. C., Choi, H., and Liao, H.: Control of particulate nitrate air pollution in
656 China, Nature Geoscience, 14, 389-395, 10.1038/s41561-021-00726-z, 2021.

657 Zhang, L., Chen, Y., Zhao, Y., Henze, D. K., Zhu, L., Song, Y., Paulot, F., Liu, X., Pan, Y., Lin, Y., and
658 Huang, B.: Agricultural ammonia emissions in China: reconciling bottom-up and top-down estimates,
659 Atmospheric Chemistry and Physics, 18, 339-355, 10.5194/acp-18-339-2018, 2018.

660 Zhang, X., Wu, Y., Liu, X., Reis, S., Jin, J., Dragosits, U., Van Damme, M., Clarisse, L., Whitburn, S.,
661 Coheur, P. F., and Gu, B.: Ammonia Emissions May Be Substantially Underestimated in China,
662 Environ Sci Technol, 51, 12089-12096, 10.1021/acs.est.7b02171, 2017.

663 Zhao, Y., Duan, L., Xing, J., Larssen, T., Nielsen, C. P., and Hao, J.: Soil acidification in China: is
664 controlling SO2 emissions enough?, 2009.

665 Zhao, Y., Zhang, L., Chen, Y., Liu, X., Xu, W., Pan, Y., and Duan, L.: Atmospheric nitrogen deposition
666 to China: A model analysis on nitrogen budget and critical load exceedance, Atmospheric Environment,
667 153, 32-40, 10.1016/j.atmosenv.2017.01.018, 2017.

668